THE CHEMICAL COMPOSITION OF RED GIANT BRANCH STARS IN THE GALACTIC GLOBULAR CLUSTERS NGC 6342 AND NGC 6366

CHRISTIAN I. JOHNSON[1,5], NELSON CALDWELL[1], R. MICHAEL RICH[2], CATHERINE A. PILACHOWSKI[3], AND TIFFANY HSYU[4]

[1] Harvard–Smithsonian Center for Astrophysics, 60 Garden Street, MS-15, Cambridge, MA 02138, USA; cjohnson@cfa.harvard.edu, ncaldwell@cfa.harvard.edu
[2] Department of Physics and Astronomy, UCLA, 430 Portola Plaza, Box 951547, Los Angeles, CA 90095-1547, USA; rmr@astro.ucla.edu
[3] Astronomy Department, Indiana University Bloomington, Swain West 319, 727 East 3rd Street, Bloomington, IN 47405-7105, USA; cpilacho@indiana.edu
[4] UCO/Lick Observatory, University of California, 1156 High Street, Santa Cruz, CA 95064, USA; thsyu@ucsc.edu

ABSTRACT

We present radial velocities and chemical abundances for red giant branch stars in the Galactic bulge globular clusters NGC 6342 and NGC 6366. The velocities and abundances are based on measurements of high-resolution ($R \gtrsim 20{,}000$) spectra obtained with the MMT–Hectochelle and WIYN–Hydra spectrographs. We find that NGC 6342 has a heliocentric radial velocity of $+112.5 \, \mathrm{km \, s^{-1}}$ ($\sigma = 8.6 \, \mathrm{km \, s^{-1}}$), NGC 6366 has a heliocentric radial velocity of $-122.3 \, \mathrm{km \, s^{-1}}$ ($\sigma = 1.5 \, \mathrm{km \, s^{-1}}$), and both clusters have nearly identical metallicities ([Fe/H] ≈ -0.55). NGC 6366 shows evidence of a moderately extended O–Na anti-correlation, but more data are needed for NGC 6342 to determine if this cluster also exhibits the typical O–Na relation likely found in all other Galactic globular clusters. The two clusters are distinguished from similar metallicity field stars as having larger [Na/Fe] spreads and enhanced [La/Fe] ratios, but we find that NGC 6342 and NGC 6366 display α and Fe-peak element abundance patterns that are typical of other metal-rich ([Fe/H] > -1) inner Galaxy clusters. However, the median [La/Fe] abundance may vary from cluster-to-cluster.

Key words: globular clusters: general – globular clusters: individual (NGC 6342, NGC 6366) – stars: abundances

Supporting material: machine-readable tables

1. INTRODUCTION

Globular cluster systems offer insights into a galaxy's chemical evolution, star formation history, dynamical evolution, and merger history. In the Milky Way, globular clusters are often categorized based on characteristics such as chemical composition, age, horizontal branch morphology, and kinematics. The observed metallicity distribution function of Galactic globular clusters is largely bimodal with approximately two-thirds of clusters belonging to a metal-poor group that peaks near [Fe/H][6] ~ -1.5 and one-third of clusters belonging to a metal-rich group that peaks near [Fe/H] ~ -0.5 (e.g., Freeman & Norris 1981; Zinn 1985; Bica et al. 2006). Furthermore, while metal-poor globular clusters are distributed across a wide range of galactocentric radii and are mostly associated with the Galactic halo, metal-rich clusters form a more flattened population that is concentrated near the inner few kiloparsecs of the Galaxy (e.g., Zinn 1985; van den Bergh 2003; Rossi et al. 2015). Recent work suggests that a majority of the inner Galaxy globular clusters with [Fe/H] $\gtrsim -1$ are members of the Galactic bulge/bar system (e.g., Minniti 1995; Côté 1999; Rossi et al. 2015). Interestingly, some age–metallicity relations find that the central metal-rich globular cluster population may even be coeval with, and in some cases older than (e.g., NGC 6522; Barbuy et al. 2009), some of the more metal-poor halo clusters (e.g., Marín-Franch et al. 2009; Forbes & Bridges 2010). In contrast, VandenBerg et al. (2013) find that clusters with [Fe/H] > -1 are younger than those with [Fe/H] < -1, and also do not find a strong correlation between galactocentric distance and age.

Although inner Galaxy globular clusters are not as extensively studied as their halo counterparts (e.g., see reviews by Kraft 1994; Gratton et al. 2004, 2012), several bulge clusters are known to exhibit unusual chemical and/or morphological characteristics. For example, Haute–Provence 1 (HP-1) is located near the Galactic center and is relatively metal-rich at [Fe/H] $= -1$, but the cluster contains a prominent blue horizontal branch and no red horizontal branch stars (Ortolani et al. 1997, 2011; Barbuy et al. 2006). Similarly, the bulge clusters NGC 6388 and NGC 6441 have [Fe/H] ~ -0.4 (e.g., Gratton et al. 2006, 2007; Carretta et al. 2007; Origlia et al. 2008), anomalous red giant branch (RGB) bumps (Nataf et al. 2013), and dominant red horizontal branches accompanied by very extended blue horizontal branches (e.g., Rich et al. 1997; Bellini et al. 2013). For HP-1, NGC 6388, and NGC 6441, the presence of a significant population of blue horizontal branch stars is not expected given the clusters' metallicities. In a similar sense, the bulge globular clusters NGC 6440 and NGC 6569 exhibit double red clumps that are so far observed only in near-infrared color–magnitude diagrams (Mauro et al. 2012). The underlying cause of the double red clump feature in these clusters is not yet clear, but in Terzan 5 a double red clump has been linked to multiple stellar populations with metallicities that range from [Fe/H] ~ -0.8 to $+0.3$ (Ferraro et al. 2009; Origlia et al. 2011, 2013). Detailed spectroscopic analyses by Origlia et al. (2011, 2013) have further revealed that the chemical composition of each population appears to match that found in bulge field stars, which supports the suggestion by Ferraro et al. (2009) that Terzan 5 may be a remnant primordial building block of the Galactic bulge.

The bulge globular clusters preserve chemical information about the early proto-bulge environment. Therefore, understanding the connection between the bulge clusters and the

---

[5] Clay Fellow.
[6] [A/B] $\equiv \log(N_A/N_B)_{\mathrm{star}} - \log(N_A/N_B)_\odot$ and $\log \epsilon(A) \equiv \log(N_A/N_H) + 12.0$ for elements A and B.

broader bulge/bar system is necessary for interpreting the complex chemodynamical stellar populations that currently reside in the inner Galaxy. However, only a handful of bulge clusters have been examined in detail using high-resolution spectroscopy. Contamination from the bulge field star population and strong differential reddening complicate both integrated light and color–magnitude diagram analyses of bulge globular clusters. Therefore, we provide here new composition and kinematic analyses of the moderately metal-rich bulge globular clusters NGC 6342 and NGC 6366, based on high-resolution optical spectra obtained with the MMT–Hectochelle and WIYN–Hydra spectrographs. Low-resolution spectroscopic analyses and color–magnitude diagram fits estimate that both clusters have [Fe/H] ~ −0.6 (e.g., Da Costa & Seitzer 1989; Heitsch & Richtler 1999; Valenti et al. 2004; Origlia et al. 2005a; Saviane et al. 2012; Campos et al. 2013), but only NGC 6342 has had some of its stars (4; Origlia et al. 2005a) examined via high-resolution spectroscopy. Although little is known about the chemical composition of NGC 6366, the cluster is particularly noteworthy because it has an unusual bottom-light mass function (Paust et al. 2009). NGC 6366 also has a very low velocity dispersion of ~1 km s^{-1} (Da Costa & Seitzer 1989; Rutledge et al. 1997), and may have experienced significant tidal stripping and mass loss (Paust et al. 2009).

In this paper, we examine the light odd-Z, α, Fe-peak, and heavy element abundance patterns of NGC 6342 and NGC 6366 to compare with those of similar metallicity bulge cluster and field stars. The addition of these new data to the literature will allow for an investigation of the chemical similarities and differences between bulge cluster and field stars, define the RGB sequence of each cluster, permit further investigation into whether or not the typical light element abundance variations found in nearly all metal-poor clusters extend also to metal-rich bulge clusters, and help constrain the contribution of dissolved globular clusters to the bulge field.

2. OBSERVATIONS, TARGET SELECTION, AND DATA REDUCTION

2.1. Observations and Target Selection

The spectra for this project were obtained using the Hectochelle (Szentgyorgyi et al. 2011) and Hydra (Bershady et al. 2008; Knezek et al. 2010) multi-fiber bench spectrographs mounted on the MMT 6.5 m and WIYN 3.5 m telescopes, respectively. NGC 6342 was observed with Hectochelle on 2014 June 18 and also with Hydra on 2013 June 27. However, NGC 6366 was only observed with Hydra on 2012 May 18. The Hectochelle observations consisted of a 2400 and 2065 s exposure set using the 110 line mm^{-1} Echelle grating, the "CJ26" filter, and 2×1 (spatial $\times$ dispersion) binning to achieve a resolving power of $R \equiv \lambda/\Delta\lambda \approx 38{,}000$. Similarly, the Hydra observations consisted of 3×3600 s exposures with the bench configured to use the 316 line mm^{-1} Echelle grating, the X18 filter, the red camera and fibers, and 2×1 binning to achieve a resolving power of $R \approx 18{,}000$. The spectra spanned approximately 6140–6310 Å for the Hectochelle data and 6080–6390 Å for the Hydra data.

The target stars for both clusters were selected using photometry and coordinates available through the Two Micron All Sky Survey (2MASS; Skrutskie et al. 2006) database. Since both clusters are located at relatively low Galactic latitudes near

the bulge, the fiducial RGB sequences for each cluster are hidden by the significant stellar crowding. Identifying the cluster RGB sequences is further complicated because the cluster stars and a large fraction of the outer bulge field stars share similar metallicities. Both clusters also are affected by significant reddening with NGC 6342 having $E(B - V) \approx 0.60$ and $\Delta E(B - V) \approx 0.40$ (Heitsch & Richtler 1999; Valenti et al. 2004; Alonso-García et al. 2012) and NGC 6366 having $E(B - V) \approx 0.70$ and $\Delta E(B - V) \approx 0.05$ (Alonso et al. 1997; Sarajedini et al. 2007; Paust et al. 2009; Dotter et al. 2010; Campos et al. 2013). The combination of these effects makes it difficult to know a priori which stars are true cluster members.

Therefore, we repeated the selection procedure used in Johnson et al. (2015) to identify cluster members in the bulge globular cluster NGC 6273. Briefly, we assumed the cluster RGB sequences could be reasonably well traced using only stars within 2′ of each cluster's core. The selection region was then broadened to include the effects of differential reddening, and stars were prioritized in the fiber assignment codes according to the distance between a star and the cluster core. A total of 216 fibers were placed on targets with Hectochelle for NGC 6342 and 51 fibers were placed on NGC 6342 targets with Hydra. Similarly, 51 Hydra fibers were also placed on targets for NGC 6366. The final selection of targets is illustrated in Figure 1 for NGC 6342 and Figure 2 for NGC 6366. The significantly larger differential reddening in NGC 6342 is clearly evident when comparing Figures 1 and 2, and is largely the cause of the significantly lower percentage of radial velocity members found in NGC 6342 (8%) versus NGC 6366 (37%; see also Section 4). The strict fiber-to-fiber distance restrictions of Hectochelle and Hydra contribute further to the low membership percentages because the magnetic buttons cannot be packed efficiently near the cluster cores, where the field contamination is at a minimum. The star identifications, J2000 coordinates, 2MASS photometry, and radial velocity measurements for all member and non-member stars are provided in Tables 1–2.

2.2. Data Reduction

The data reduction process for both the Hectochelle and Hydra spectra was carried out using standard IRAF[7] tasks. The raw spectra were bias subtracted and trimmed before the more specialized tasks of aperture identification and tracing, scattered light removal, flat-field correction, ThAr wavelength calibration, cosmic-ray removal, spectrum extraction, and sky subtraction were carried out. Note that the sky subtraction was performed using simultaneous sky spectra obtained with fibers placed on "blank" sky regions in the Hectochelle and Hydra fields of view. While a majority of the Hydra data reduction was performed using the IRAF task *dohydra*, most of the Hectochelle reduction procedures were carried out by a dedicated pipeline maintained at the Smithsonian Astrophysical Observatory's Telescope Data Center.

The final data reduction steps of telluric subtraction, continuum fitting, and spectrum combining were carried out using the IRAF tasks *telluric*, *continuum*, and *scombine* outside the general pipelines. The final combined spectra yielded

---

[7] IRAF is distributed by the National Optical Astronomy Observatory, which is operated by the Association of Universities for Research in Astronomy, Inc., under cooperative agreement with the National Science Foundation.
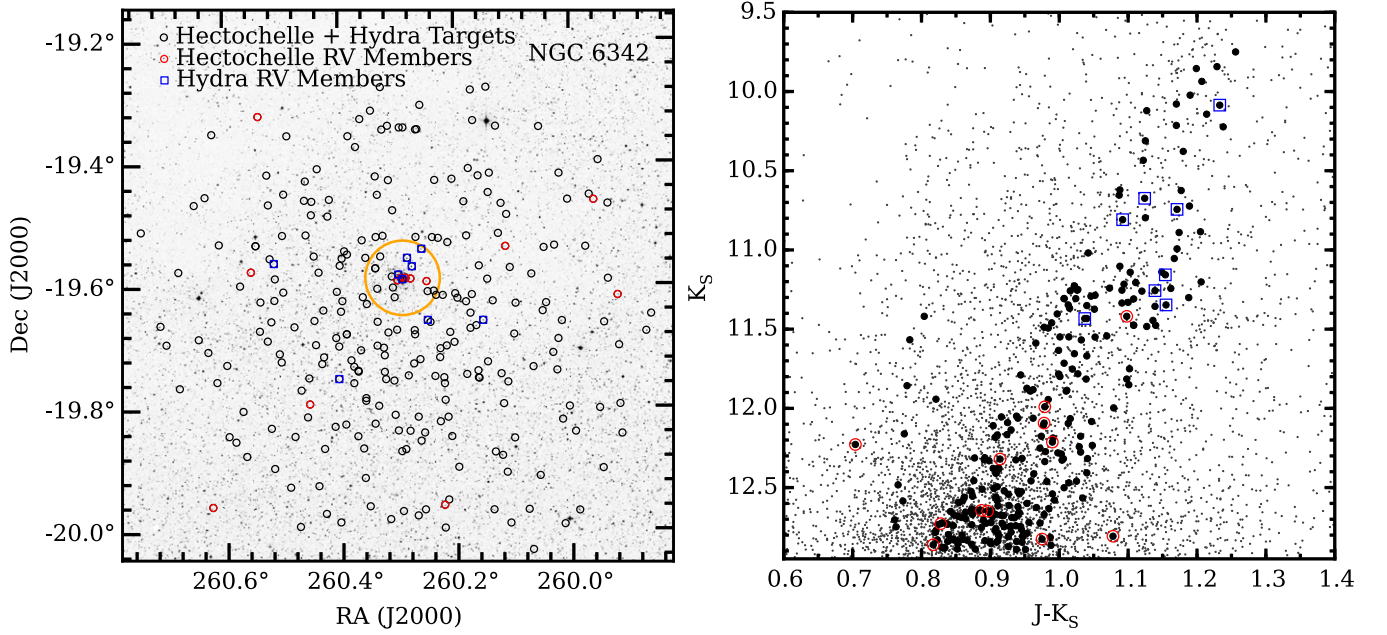
Figure 1. Left: a Second Palomar Observatory Sky Survey r-band image of NGC 6342 is shown, and the open black circles designate the coordinates of all stars observed with MMT–Hectochelle and WIYN–Hydra. The open red circles (Hectochelle) and open blue boxes (Hydra) indicate the stars that have radial velocities consistent with cluster membership. The solid orange contour line illustrates a distance of five times the cluster's 0.73 half-light radius (Harris 1996; 2010 version). Right: A K_S vs. $J - K_S$ color–magnitude diagram is shown for targets within $30'$ of NGC 6342. The small filled gray circles are all of the stars from the 2MASS database (Skrutskie et al. 2006). The red and blue symbols are the same as in the left panel, and the filled black circles indicate all stars that were observed with both instruments. Note that the two stars 2MASS 17220959–1919193 and 2MASS 17223024–1957315 have velocities that may be consistent with cluster membership but are significantly bluer and redder than the main giant branch.
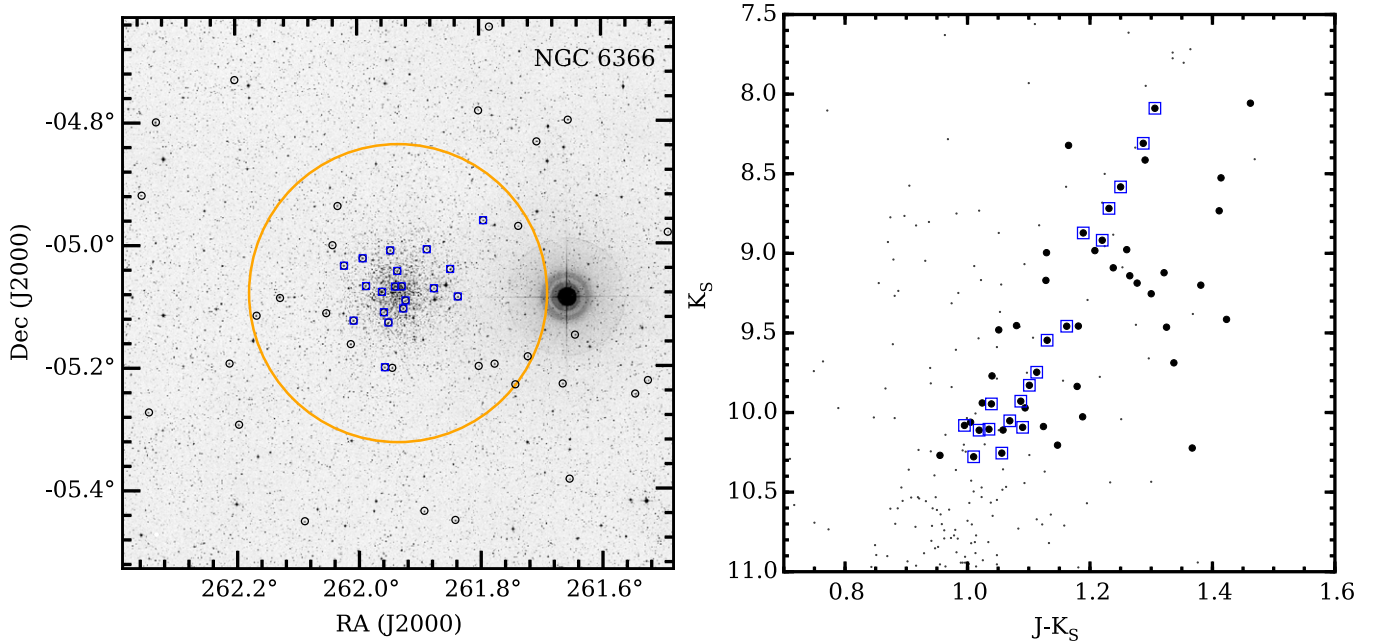
Figure 2. Left: similar to Figure 1, the open black circles show the coordinates for all stars near NGC 6366 that were observed with the WIYN–Hydra instrument. The targets that have radial velocities consistent with cluster membership are designated by open blue boxes. The solid orange contour line illustrates a distances of 5 times the cluster's 2.92 half-light radius (Harris 1996; 2010 version). Right: A K_S vs. $J - K_S$ color–magnitude diagram is shown for targets within $30'$ of NGC 6366. The small filled gray circles are all stars from the 2MASS database (Skrutskie et al. 2006). The black and blue symbols are the same as those in Figure 1.

signal-to-noise ratios (S/Ns) of approximately 50–100 per resolution element. Due to higher extinction, worse observing conditions, and shorter exposures (for Hectochelle), the NGC 6342 data tended to have lower S/Ns than the NGC 6366 data. However, we only measured abundances in stars with the highest quality spectra, and for which we could measure >10 Fe I lines (see Table 3).

3. DATA ANALYSIS

3.1. Model Atmospheres

The model atmosphere parameters effective temperature ($T_{\rm eff}$), metallicity ([M/H]), and microturbulence ($\xi_{\rm mic.}$) were determined using spectroscopic methods. Specifically, temperatures were set by removing any trends in plots of $\log \epsilon({\rm Fe\,I})$

Table 1
NGC 6342 Coordinates, Photometry, and Velocities

Star Name (2MASS)	R.A. (J2000) (Degrees)	decl. (J2000) (Degrees)	J (mag)	H (mag)	K_S (mag)	RV_{helio} (km s^{-1})	RV Error (km s^{-1})
Hectochelle Probable Members							
17194058−1937038	259.919111	−19.617743	13.531	12.862	12.644	+102.06	0.30
17195030−1927431	259.959610	−19.461985	13.234	12.509	12.320	+121.84	0.26
Hectochelle Probable Non-members							
17192669−1938549	259.861219	−19.648594	13.622	12.915	12.721	−67.94	0.33
17212139−1934169[a]	260.339162	−19.571383	12.314	11.522	11.307	+2.36	0.21
Hydra Probable Members							
17203668−1939270	260.152851	−19.657518	11.798	10.868	10.674	+110.01	0.28
17205974−1939237	260.248945	−19.656588	11.319	10.451	10.086	+98.28	0.71
Hydra Probable Non-members							
17201119−1932228	260.046651	−19.539692	12.317	11.456	11.206	+32.13	0.40
17212139−1934169[a]	260.339162	−19.571383	12.314	11.522	11.307	+1.25	0.22

Note.
[a] This flag indicates that the star was observed with both the Hectochelle and Hydra instruments.

(This table is available in its entirety in machine-readable form.)

Table 2
NGC 6366 Coordinates, Photometry, and Velocities

Star Name (2MASS)	R.A. (J2000) (Degrees)	decl. (J2000) (Degrees)	J (mag)	H (mag)	K_S (mag)	RV_{helio} (km s^{-1})	RV Error (km s^{-1})
Hydra Probable Members							
17271061−0457415	261.794225	−4.961547	11.016	10.189	9.929	−121.91	0.21
17272071−0505087	261.836299	−5.085757	11.288	10.482	10.278	−122.47	0.21
17272367−0502272	261.848632	−5.040897	10.138	9.200	8.918	−121.24	0.22
17273010−0504197	261.875443	−5.072152	10.860	9.994	9.747	−123.89	0.22
17273285−0500304	261.886891	−5.008450	11.140	10.316	10.105	−119.99	0.22
Hydra Probable Non-members							
17255789−0458546	261.491242	−4.981845	10.464	9.482	9.187	+40.71	0.40
17260595−0513249	261.524819	−5.223611	11.025	10.013	9.688	−117.14	0.36
17261100−0514439	261.545871	−5.245550	10.534	9.692	9.454	+43.06	0.19
17263463−0508564	261.644297	−5.149007	11.352	10.435	10.205	+25.02	0.20
17263699−0523021	261.654149	−5.383922	10.810	9.944	9.770	+54.68	0.18

(This table is available in its entirety in machine-readable form.)

abundance versus excitation potential, and microturbulence values were set by removing any trends in plots of $\log \epsilon(\mathrm{Fe\,I})$ abundance versus reduced equivalent width[8] (EW). The model atmosphere metallicities were set to the measured [Fe/H] values.

In Figure 3, we compare the spectroscopic T_{eff} values derived using excitation equilibrium with the $J − K_S$ color–temperature relation provided by González Hernández & Bonifacio (2009), assuming $E(B − V) = 0.57$ for NGC 6342 (Valenti et al. 2004) and $E(B − V) = 0.70$ for NGC 6366 (Alonso et al. 1997). Despite the presence of significant differential reddening in both clusters, the two temperature scales are well-correlated. We find an average offset (ΔT_{eff}), in the sense of photometric T_{eff} minus spectroscopic T_{eff}, to be $\Delta T_{eff} = −32$ K ($\sigma = 138$ K) for NGC 6342 and $\Delta T_{eff} = +77$ K ($\sigma = 131$ K) for NGC 6366. Although the agreement is

comparable to the 94 K standard deviation of the color–temperature relation (see González Hernández & Bonifacio 2009; their Table 5), the removal of one significant outlier in NGC 6342 and two significant outliers in NGC 6366 decreases the offsets to $\Delta T_{eff} = +32$ K ($\sigma = 77$ K) and $\Delta T_{eff} = +33$ K ($\sigma = 83$ K), respectively.

Since the data span a limited wavelength range, we did not constrain surface gravities ($\log(g)$) by setting ionization equilibrium between neutral and singly ionized species (e.g., Fe I/II). Instead, we estimated surface gravities using isochrones available through the Dartmouth Stellar Evolution database (Dotter et al. 2008). We used the online interpolator[9] to obtain a surface gravity value for each star, given its spectroscopically determined temperature. We assumed a

---

[8] The reduced equivalent width is defined as $\log(EW/\lambda)$.

[9] The Dartmouth Stellar Evolution database online interpolator can be accessed at http://stellar.dartmouth.edu/models/isolf_new.html.

Table 3
NGC 6342 and NGC 6366 Stellar Atmosphere Parameters and Abundance Ratios

Star Name (2MASS)	$T_{\rm eff}$ (K)	log(g) (cgs)	[Fe/H] (dex)	$\xi_{\rm mic.}$ (km s^{-1})	[O/Fe] (dex)	[Na/Fe] (dex)	[Mg/Fe] (dex)	[Si/Fe] (dex)	[Ca/Fe] (dex)	[Cr/Fe] (dex)	[Ni/Fe] (dex)	[La/Fe] (dex)
NGC 6342												
17205345−1957303	4600	2.20	−0.41	2.05	⋯	−0.16	⋯	+0.32	+0.15	⋯	−0.04	+0.28
17210009−1935354	4200	1.50	−0.59	1.70	+0.45	+0.17	⋯	+0.44	⋯	⋯	+0.00	−0.05
17210680−1935191	4850	2.75	−0.49	1.55	⋯	−0.08	⋯	+0.49	+0.22	⋯	−0.04	+0.31
17211185−1934551	4175	1.40	−0.65	2.20	+0.77	+0.02	+0.37	+0.41	+0.29	−0.13	+0.10	+0.12
NGC 6366												
17271061−0457415	4575	2.15	−0.66	2.00	+0.67	+0.46	+0.36	+0.35	+0.40	+0.16	+0.12	+0.33
17272071−0505087	4650	2.45	−0.47	1.90	+0.57	+0.03	+0.26	+0.22	+0.22	−0.21	+0.09	+0.29
17273010−0504197	4400	1.80	−0.47	1.60	+0.27	+0.27	+0.29	+0.21	+0.33	−0.04	⋯	+0.14
17273285−0500304	4375	1.75	−0.63	1.70	+0.60	−0.11	+0.30	+0.35	+0.17	⋯	+0.15	+0.00
17274128−0505308	4550	2.05	−0.60	1.65	+0.58	+0.21	+0.37	+0.23	+0.44	−0.03	+0.02	+0.17
17274221−0506173	4400	1.65	−0.67	2.15	+0.67	+0.25	+0.41	+0.18	+0.48	+0.17	+0.18	+0.19
17274279−0504077	4475	2.00	−0.42	1.70	+0.43	+0.18	+0.14	+0.35	+0.31	−0.13	+0.10	+0.19
17274541−0504089	4500	1.95	−0.62	1.80	+0.52	+0.27	+0.34	+0.26	+0.38	+0.09	+0.07	+0.26
17274724−0500362	4350	1.75	−0.47	1.90	+0.40	+0.12	+0.14	+0.44	+0.20	⋯	+0.05	+0.09
17274809−0507395	4525	2.10	−0.52	1.65	+0.32	+0.38	+0.34	+0.33	+0.37	+0.08	+0.01	+0.24
17274982−0506395	4475	1.60	−0.60	1.75	+0.60	−0.09	+0.27	+0.25	+0.19	−0.24	+0.15	+0.14
17275683−0504051	4400	1.75	−0.62	1.90	+0.59	+0.06	+0.34	+0.18	+0.31	−0.02	+0.09	+0.19
17280180−0507277	4550	2.15	−0.41	1.65	+0.36	+0.04	+0.23	+0.34	+0.16	⋯	+0.14	+0.13

standard helium mass fraction, [α/Fe] = +0.4 (Origlia et al. 2005a; see also Section 5), and an age of 11 Gyr for both clusters (e.g., Campos et al. 2013; VandenBerg et al. 2013).

Each model atmosphere was calculated by interpolating within the α-enhanced ATLAS9 grid (Castelli & Kurucz 2004).[10] The final values were determined by simultaneously solving for temperature, metallicity, and microturbulence and iteratively redetermining surface gravity via the isochrone interpolator mentioned above. The final adopted parameters for NGC 6342 (4 stars) and NGC 6366 (13 stars) are provided in Table 3.

3.2. Abundance Analysis

The abundance analysis for this work closely follows that described in Johnson et al. (2014). Briefly, the abundances of Si, Ca, Cr, Fe, and Ni were calculated using the *abfind* driver of the LTE line analysis code MOOG (Sneden 1973; 2014 version). Similarly, the abundances of O, Na, Mg, and La were determined using the *synth* driver of MOOG to minimize differences between the observed and synthetic spectra. All EWs were measured using the semi-automated code outlined in Johnson et al. (2014) that fits single or multiple Gaussian profiles to isolated and blended absorption lines.

Since previous estimates indicate that both clusters should have [Fe/H] ∼ −0.6 (see Section 1), we performed a differential abundance analysis relative to the giant star Arcturus ([Fe/H] ≈ −0.5; e.g., Ramírez & Allende Prieto 2011). The line list provided in Table 4 uses the same log(*gf*) values, solar reference abundances, and Arcturus reference abundances as those in Johnson et al. (2014), but we added a few additional Fe I lines due to differences in wavelength coverage between the FLAMES, Hectochelle, and Hydra data. The only other exception to the Johnson et al. (2014) line list was our inclusion
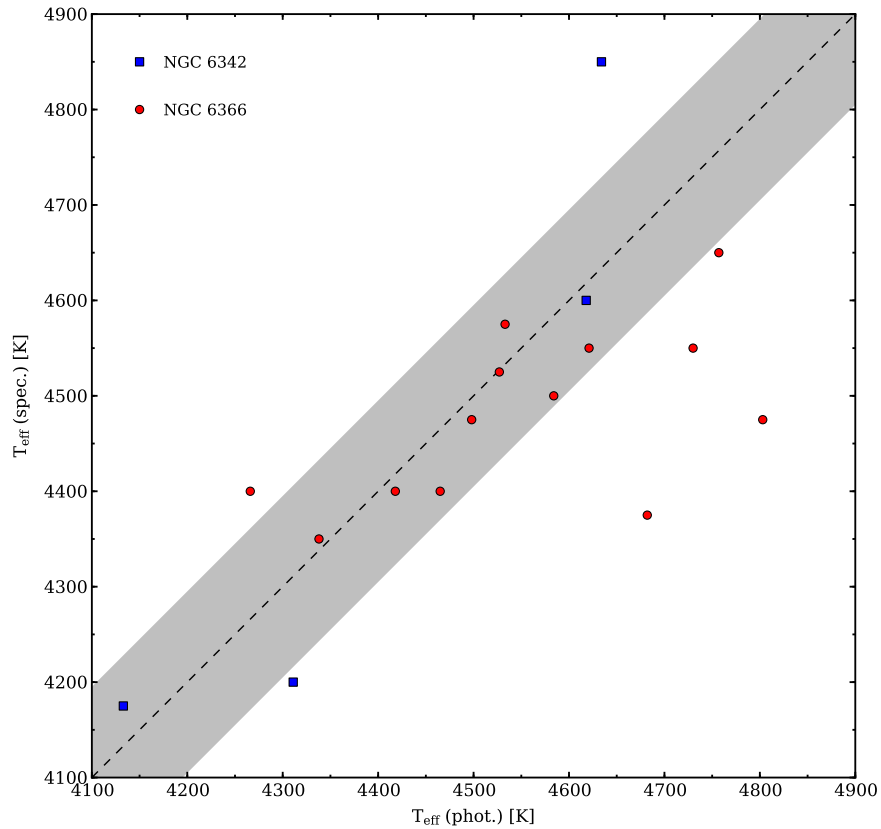
of the La atomic data from Lawler et al. (2001), which takes into account hyperfine structure introduced by the ^{139}La isotope.

For the abundances determined by spectrum synthesis, we included atomic lines from the Kurucz database[11] and CN molecular lines from Sneden et al. (2014). The original log(*gf*) values were manually adjusted until the synthetic spectrum matched the observed spectrum of the Arcturus atlas (Hinkle et al. 2000). We adopted the model atmosphere parameters and Arcturus abundances listed in Table 4 and Ramírez & Allende Prieto (2011) for C, N, O, Na, Mg, and La. In order to account for contributions from CN lines, we initially assumed the stars were well-mixed with [C/Fe] = –0.30, [N/Fe] = +0.50, and ^{12}C/^{13}C = 4, which are typical values for evolved RGB stars in the bulge field and clusters (e.g., Origlia et al. 2005a; Meléndez et al. 2008; Ryde et al. 2010). Since C, N, and O are integral parts of the molecular equilibrium calculations, we first fit the 6300 [O I] line and nearby CN features to define the oxygen and C + N abundances for each star. The nitrogen abundance was treated as a free parameter in order to fit the CN line profiles. For the two stars in NGC 6342 that we were not able to measure [O/Fe], we assumed [O/Fe] = +0.60, the average oxygen abundance for the other two NGC 6342 stars in our sample, and set [C/Fe] = –0.30 and [N/Fe] = +0.50.

While the 6154/6160 Å Na I and 6262 Å La II lines are relatively uncontaminated, the 6318–6319 Å Mg I triplet lines are moderately affected by a broad Ca I auto-ionization feature. In order to correct for this effect, we adjusted the log ϵ(Ca) abundance until the shape of the synthetic and observed spectra matched in the nearby continuum windows (e.g., see Figure 6 of Johnson et al. 2014). The log ϵ(Ca) abundance that best reproduced the auto-ionization feature tended to be ∼0.3–0.4 dex less than the average log ϵ(Ca) abundance measured from the individual atomic lines.

---

[10] The model atmosphere grid can be accessed at http://wwwuser.oats.inaf.it/castelli/grids.html.

[11] The most up-to-date line lists can be accessed at http://kurucz.harvard.edu/linelists/gfnew/.

Figure 3. Comparison between the effective temperatures derived by enforcing excitation equilibrium of Fe I ($T_{\rm eff}$ spec.) and using the $J - K_{\rm S}$ color–temperature relation ($T_{\rm eff}$ phot.) from González Hernández & Bonifacio (2009) for NGC 6342 (filled red circles) and NGC 6366 (filled blue boxes). The dashed black line indicates perfect agreement, and the shaded region illustrates the 1σ temperature uncertainty from González Hernández & Bonifacio (2009).

3.2.1. Internal Abundance Uncertainties

The largest sources of internal abundance uncertainties are typically related to the derivation of the stellar model atmosphere parameters. Additional sources, such as line blending, continuum placement, atomic parameters, and visual profile fitting, tend to have only a small effect on the final abundances derived from moderately high S/N and resolution spectra. The line profile fitting code used for this project takes into account a spectrum's S/N and estimates the uncertainty range in continuum placement. The continuum uncertainty is then propagated through the profile fitting procedure, and the code generates an EW error estimate for every line. The average EW uncertainty ranges from approximately 10% for a line of 20 mÅ to 2% for a line of 150 mÅ. These uncertainties translate into abundance errors of ∼0.02–0.05 dex, which are comparable to the typical standard errors of the mean derived in our analysis (∼0.03 dex on average). Therefore, our final internal uncertainty calculations provided in Table 5 include the error of the mean for each element as a tracer of the random measurement error.

In order to examine the internal sensitivity of the derived log ϵ(X) abundances to changes in the model atmosphere parameters, we calculated the abundance differences between the "best-fit" model and those with each parameter adjusted within its estimated uncertainty range. A temperature uncertainty of 75 K was adopted based on a comparison of the spectroscopic and photometric $T_{\rm eff}$ values shown in Figure 3, where the 1σ star-to-star deviation, after removing three extreme outliers, is 79 K. Since the surface gravity values were determined from the isochrones described in Section 3.1, we estimated that the interpolation uncertainty for log(g) was 0.10 cgs, assuming

$\Delta T_{\rm eff} = 75$ K and Δage $= 1$ Gyr. The overall metallicity uncertainty was estimated to be 0.10 dex based on the star-to-star dispersion in our derived [Fe/H] values for both clusters. Finally, we estimated that the microturbulence velocity uncertainty was 0.10 km s^{-1}, based on an examination of the line-to-line scatter in plots of log ϵ(Fe I) abundance versus reduced EW. The final abundance uncertainties, including the measurement errors described above, were added in quadrature to produce the final uncertainty values listed in Table 5. Note that the [X/Fe] ratios take into account both the errors in [Fe/H] and [X/H] for each element. The typical errors range from ∼0.05 to 0.10 dex.

4. RADIAL VELOCITY MEASUREMENTS AND CLUSTER MEMBERSHIP

The radial velocities for both NGC 6342 and NGC 6366 were measured using the IRAF task *fxcor*, which cross correlated the observed spectra with a convolved and rebinned version of the Arcturus atlas (Hinkle et al. 2000) that matches the resolution and sampling of the Hectochelle and Hydra spectra. We avoided contamination due to any residual telluric lines by only using the 6120–6275 Å region for the cross correlation. The heliocentric corrections were determined using the information in the image headers and the IRAF task *rvcor*. Since there were two exposures for the Hectochelle data and three exposures each for the Hydra data, we measured the heliocentric radial velocity (RV$_{\rm helio}$) in each exposure and treated these values as independent measurements. The standard deviation of these measurements for each star are listed in Tables 1–2 as the RV$_{\rm helio}$ errors. The average RV$_{\rm helio}$ error for the entire sample is 0.38 km s^{-1} ($\sigma = 0.31$ km s^{-1});

Table 4
Line List and Adopted Reference Abundances

Species	Wavelength (Å)	E.P. (eV)	log(gf)[a]	log ϵ(X)$_\odot$ (dex)	log ϵ(X)$_{Arc.}$ (dex)	[X/Fe] or [Fe/H]$_{Arc.}$ (dex)
[O I]	6300.30	0.00	−9.750	8.69	8.63	+0.44
Na I	6154.23	2.10	−1.560	6.33	5.89	+0.06
Na I	6160.75	2.10	−1.210	6.33	5.89	+0.06
Mg I	6318.71	5.10	−2.010	7.58	7.38	+0.30
Mg I	6319.24	5.10	−2.250	7.58	7.38	+0.30
Mg I	6319.49	5.10	−2.730	7.58	7.38	+0.30
Si I	6142.48	5.62	−1.575	7.55	7.38	+0.33
Si I	6145.02	5.62	−1.460	7.55	7.38	+0.33
Si I	6155.13	5.62	−0.774	7.55	7.38	+0.33
Si I	6155.69	5.62	−2.352	7.55	7.38	+0.33
Si I	6195.43	5.87	−1.560	7.55	7.38	+0.33
Si I	6237.32	5.61	−1.115	7.55	7.38	+0.33
Si I	6244.47	5.62	−1.303	7.55	7.38	+0.33
Ca I	6122.22	1.89	−0.466	6.36	6.07	+0.21
Ca I	6156.02	2.52	−2.637	6.36	6.07	+0.21
Ca I	6161.30	2.52	−1.246	6.36	6.07	+0.21
Ca I	6162.17	1.90	−0.210	6.36	6.07	+0.21
Ca I	6166.44	2.52	−1.262	6.36	6.07	+0.21
Ca I	6169.04	2.52	−0.837	6.36	6.07	+0.21
Ca I	6169.56	2.53	−0.628	6.36	6.07	+0.21
Cr I	6330.09	0.94	−3.000	5.67	5.09	−0.08
Fe I	6094.37	4.65	−1.700	7.52	7.02	−0.50
Fe I	6100.27	4.56	−2.116	7.52	7.02	−0.50
Fe I	6151.62	2.18	−3.379	7.52	7.02	−0.50
Fe I	6159.37	4.61	−1.950	7.52	7.02	−0.50
Fe I	6165.36	4.14	−1.584	7.52	7.02	−0.50
Fe I	6173.33	2.22	−2.930	7.52	7.02	−0.50
Fe I	6180.20	2.73	−2.629	7.52	7.02	−0.50
Fe I	6187.99	3.94	−1.690	7.52	7.02	−0.50
Fe I	6200.31	2.61	−2.437	7.52	7.02	−0.50
Fe I	6219.28	2.20	−2.563	7.52	7.02	−0.50
Fe I	6229.23	2.85	−2.885	7.52	7.02	−0.50
Fe I	6232.64	3.65	−1.263	7.52	7.02	−0.50
Fe I	6240.65	2.22	−3.353	7.52	7.02	−0.50
Fe I	6252.56	2.40	−1.847	7.52	7.02	−0.50
Fe I	6253.83	4.73	−1.500	7.52	7.02	−0.50
Fe I	6270.22	2.86	−2.649	7.52	7.02	−0.50
Fe I	6315.81	4.08	−1.720	7.52	7.02	−0.50
Fe I	6322.69	2.59	−2.446	7.52	7.02	−0.50
Fe I	6330.85	4.73	−1.230	7.52	7.02	−0.50
Fe I	6335.33	2.20	−2.387	7.52	7.02	−0.50
Fe I	6336.82	3.69	−0.866	7.52	7.02	−0.50
Ni I	6128.96	1.68	−3.400	6.25	5.81	+0.06
Ni I	6130.13	4.27	−1.040	6.25	5.81	+0.06
Ni I	6175.36	4.09	−0.619	6.25	5.81	+0.06
Ni I	6176.81	4.09	−0.270	6.25	5.81	+0.06
Ni I	6177.24	1.83	−3.550	6.25	5.81	+0.06
Ni I	6186.71	4.11	−0.890	6.25	5.81	+0.06
Ni I	6191.17	1.68	−2.233	6.25	5.81	+0.06
Ni I	6223.98	4.11	−0.960	6.25	5.81	+0.06
Ni I	6322.16	4.15	−1.190	6.25	5.81	+0.06
La II	6262.29	0.40	hfs	1.13	0.57	−0.06

Note.
[a] The "hfs" designation indicates that the abundance was calculated by taking hyperfine structure into account. See text for details.

however, the Hectochelle data have a higher resolution and thus a lower average error of 0.35 km s^{-1} ($\sigma = 0.20$ km s^{-1}) compared to the 0.44 km s^{-1} ($\sigma = 0.45$ km s^{-1}) average error for the Hydra data.

Three stars in the field of NGC 6342 (2MASS 17221115–1931581, 17213359–1940422, and 17212139–1934169) were observed with both Hectochelle and Hydra (see also Table 1), and the independent RV$_{helio}$ measurements permit a rough estimate of the zero point offset between the two observing runs. The RV$_{helio}$ differences, in the sense of Hectochelle minus Hydra, are +0.18 km s^{-1}, +6.10 km s^{-1}, and +1.11 km s^{-1} for 2MASS 17221115–1931581, 17213359–1940422, and

Table 5
NGC 6342 and NGC 6366 Abundance Ratio Uncertainties

Star Name (2MASS)	Δ[Fe/H] (dex)	Δ[O/Fe] (dex)	Δ[Na/Fe] (dex)	Δ[Mg/Fe] (dex)	Δ[Si/Fe] (dex)	Δ[Ca/Fe] (dex)	Δ[Cr/Fe] (dex)	Δ[Ni/Fe] (dex)	[ΔLa/Fe] (dex)
				NGC 6342					
17205345−1957303	0.05	⋯	0.09	⋯	0.08	0.12	⋯	0.09	0.09
17210009−1935354	0.06	0.10	0.10	⋯	0.10	⋯	⋯	0.13	0.10
17210680−1935191	0.06	⋯	0.09	⋯	0.09	0.13	⋯	0.09	0.09
17211185−1934551	0.04	0.08	0.09	0.05	0.07	0.12	0.13	0.10	0.08
				NGC 6366					
17271061−0457415	0.05	0.09	0.07	0.08	0.12	0.09	0.11	0.07	0.09
17272071−0505087	0.05	0.09	0.06	0.07	0.08	0.09	0.11	0.07	0.09
17273010−0504197	0.06	0.10	0.08	0.06	0.09	0.11	0.13	⋯	0.09
17273285−0500304	0.06	0.10	0.07	0.06	0.09	0.11	⋯	0.11	0.09
17274128−0505308	0.06	0.10	0.07	0.08	0.08	0.09	0.12	0.11	0.09
17274221−0506173	0.05	0.09	0.07	0.08	0.08	0.10	0.12	0.08	0.09
17274279−0504077	0.07	0.10	0.08	0.07	0.11	0.10	0.13	0.09	0.10
17274541−0504089	0.05	0.09	0.07	0.05	0.07	0.09	0.12	0.08	0.09
17274724−0500362	0.06	0.10	0.08	0.08	0.09	0.11	⋯	0.09	0.09
17274809−0507395	0.06	0.09	0.10	0.06	0.11	0.10	0.12	0.09	0.09
17274982−0506395	0.07	0.10	0.10	0.07	0.08	0.10	0.12	0.10	0.10
17275683−0504051	0.05	0.09	0.09	0.11	0.09	0.09	0.12	0.07	0.09
17280180−0507277	0.06	0.10	0.08	0.09	0.07	0.10	⋯	0.09	0.10

17212139–1934169, respectively. If we neglect the large RV$_{helio}$ difference for 2MASS 17213359–1940422, which could be a velocity variable or binary star, the average zero point offset between Hectochelle and Hydra is +0.65 km s^{-1}.

Given the significant stellar crowding, differential reddening, and similar metallicities of bulge field stars to the NGC 6342 and NGC 6366 cluster stars, radial velocities are useful indicators of cluster membership. Previous analyses measured heliocentric radial velocities of NGC 6342 that range from ∼+114 to +118 km s^{-1} with velocity dispersions that range from ∼5 to 8 km s^{-1} (Dubath et al. 1997; Origlia et al. 2005a; Casetti-Dinescu et al. 2010). Similarly, the heliocentric radial velocity estimates for NGC 6366 range from −122.6 to −123.2 km s^{-1}, but the dispersion is estimated to be only ∼1 km s^{-1} (Da Costa & Seitzer 1989; Rutledge et al. 1997). We find in agreement with past work that the average RV$_{helio}$ of NGC 6342 is +112.5 km s^{-1} ($\sigma = 8.6$ km s^{-1}) and that of NGC 6366 is −122.3 km s^{-1} ($\sigma = 1.5$ km s^{-1}).

Although the broad radial velocity distribution of the bulge field stars is consistent with observations from recent large sample studies (e.g., Kunder et al. 2012; Ness et al. 2013; Zoccali et al. 2014), the field contamination makes assigning membership more difficult in the NGC 6342 field than the NGC 6366 field (see Figure 4). Therefore, we have only included stars with RV$_{helio}$ values between 95–130 km s^{-1} (∼2σ) as possible cluster members for NGC 6342. Nevertheless, as mentioned in Section 2.1, only 8% and 37% of the observed targets are likely radial velocity members of NGC 6342 and NGC 6366, respectively. However, a high contamination rate of field stars is typical for bulge globular cluster observations that extend far beyond the cluster core (e.g., Gratton et al. 2007).

5. RESULTS AND DISCUSSION

5.1. Comparing NGC 6342 and NGC 6366

As mentioned in Section 1, neither NGC 6342 nor NGC 6366 has been extensively studied with high-resolution spectroscopy.

Origlia et al. (2005a) obtained high-resolution infrared spectra of four RGB stars in NGC 6342 and found the cluster to be only moderately metal-poor (⟨[Fe/H]⟩ = −0.60), enhanced in all α-elements (⟨[α/Fe]⟩ = +0.34), and exhibit a small star-to-star dispersion in [O/Fe] (Δ[O/Fe] = 0.04 dex). NGC 6366 has never been analyzed with high-resolution spectroscopy, but photometric analyses suggest that the cluster may host at least two populations with different light element chemistry (Piotto et al. 2015; their Figure 14). Photometric and low-/moderate-resolution spectroscopy further indicate that NGC 6366 is comparable in metallicity to NGC 6342, with estimates ranging from [Fe/H] = −0.85 to −0.54 (Johnson et al. 1982; Da Costa & Seitzer 1989; Da Costa & Armandroff 1995; Alonso et al. 1997; Dotter et al. 2010; Saviane et al. 2012; Campos et al. 2013).

The chemical composition results presented here, including 4 RGB stars for NGC 6342 and 13 RGB stars for NGC 6366, are in general agreement with previous work. For NGC 6342, we find an average [Fe/H] = −0.53 ($\sigma = 0.11$), significantly enhanced [O/Fe] (⟨[O/Fe]⟩ = +0.61) with smaller enhancements for the heavier α-elements (⟨[α/Fe]⟩ = +0.33), and a moderate spread in [O/Fe] (Δ[O/Fe] = 0.32). For NGC 6366, we find an average [Fe/H] = −0.55 ($\sigma = 0.09$), a slightly lower average [O/Fe] = +0.51 with similar enhancements for the heavier α-elements (⟨[α/Fe]⟩ = +0.29), and a slightly larger spread in [O/Fe] (Δ[O/Fe] = 0.40). Both clusters also exhibit moderate enhancements and dispersions of [Na/Fe], and possibly [La/Fe], but the Fe-peak elements in both clusters mostly track iron.[12] The data indicate that NGC 6366 may have [Cr/Fe] and [Ni/Fe] abundances that are ∼0.1 dex higher than those of NGC 6342, but a larger sample of Fe-peak element measurements in these two clusters is needed in order to verify that this difference is real. We note that NGC 6342 and NGC 6366 have similar differences between their maximum and

---

[12] The 0.14 dex dispersion in [Cr/Fe] for NGC 6366 is likely due to increased measurement errors and the availability of only one weak line.
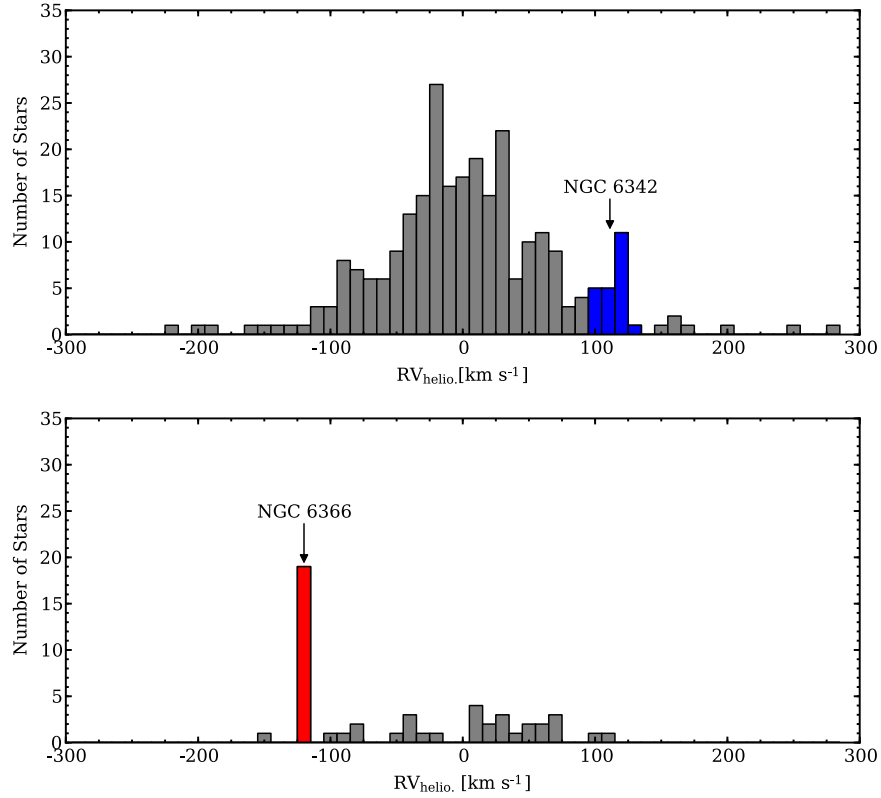
Figure 4. Heliocentric radial velocity distributions for the fields near NGC 6342 (top) and NGC 6366 (bottom) are shown with bin sizes of 10 km s^{-1}. The high probability members for each cluster are highlighted in blue for NGC 6342 and red for NGC 6366.

minimum [La/Fe] abundances (Δ[La/Fe] ~ 0.35 dex), but different dispersions. Therefore, the larger dispersion in NGC 6342 may be a result of the small sample size (four stars); however, we cannot rule out that the smaller [La/Fe] dispersion in NGC 6366 is a residual effect from enhanced tidal disruption (Paust et al. 2009). A summary of the average and dispersion values for every element in each star per cluster is provided in Table 6.

5.2. NGC 6342, NGC 6366, and the Bulge Globular Cluster System

In Figure 5, we compare the light element abundance patterns of individual stars in NGC 6342 and NGC 6366 with those of similar metallicity ($-0.7 \lesssim$ [Fe/H] $\lesssim -0.4$) bulge globular clusters. The relationships between the element ratio pairs shown in Figure 5 are often interpreted as being a result of high temperature ($T \gtrsim 65 \times 10^6$ K) proton-capture burning (e.g., Langer et al. 1993; Arnould et al. 1999; Prantzos et al. 2007; Ventura et al. 2012), and as a consequence many globular clusters exhibit O–Na and Mg–Si anti-correlations concurrent with O–Mg correlations (e.g., Yong et al. 2005, 2014; Carretta et al. 2009a; Johnson & Pilachowski 2010; Cohen & Kirby 2012; Carretta et al. 2014; Carretta 2015; Roederer & Thompson 2015). However, as can be seen in Figure 5, NGC 6366 only shows evidence supporting the existence of a moderately extended O–Na anti-correlation. Although the NGC 6342 data overlap with the O–Na trend observed in NGC 6366 and other similar metallicity bulge clusters, we were only able to measure [O/Fe] and [Na/Fe] in two stars for NGC 6342 and therefore cannot comment further

Table 6
Composition Comparison: $-0.7 \leqslant$ [Fe/H] $\leqslant -0.4$

Average [X/Fe]	NGC 6342	NGC 6366	Bulge Clusters[a]	Bulge Clusters[b]	Bulge Field
$\langle$[O/Fe]$\rangle$	+0.61	+0.51	+0.48	+0.16	+0.47
$\langle$[Na/Fe]$\rangle$	−0.01	+0.16	+0.17	+0.36	−0.01
$\langle$[Mg/Fe]$\rangle$	+0.37	+0.29	+0.39	+0.34	+0.31
$\langle$[Si/Fe]$\rangle$	+0.42	+0.28	+0.29	+0.31	+0.29
$\langle$[Ca/Fe]$\rangle$	+0.22	+0.30	+0.31	+0.22	+0.26
$\langle$[Cr/Fe]$\rangle$	−0.13	−0.02	−0.07	−0.08	+0.01
$\langle$[Ni/Fe]$\rangle$	+0.01	+0.10	−0.04	+0.02	+0.06
$\langle$[La/Fe]$\rangle$	+0.17	+0.18	⋯	+0.36	−0.20
			Abundance Dispersions		
σ[O/Fe]	0.23	0.13	0.07	0.32	0.15
σ[Na/Fe]	0.14	0.17	0.15	0.25	0.12
σ[Mg/Fe]	⋯	0.08	0.07	0.11	0.09
σ[Si/Fe]	0.07	0.08	0.09	0.12	0.11
σ[Ca/Fe]	0.07	0.11	0.10	0.16	0.11
σ[Cr/Fe]	⋯	0.14	0.03	0.18	0.10
σ[Ni/Fe]	0.07	0.05	0.05	0.09	0.05
σ[La/Fe]	0.17	0.09	⋯	0.09	0.08

Notes.
[a] NGC 6388 and NGC 6441 are omitted.
[b] All bulge globular clusters with $-0.7 \leqslant$ [Fe/H] $\leqslant -0.4$ are included.

on the extent, or existence, of a true O–Na anti-correlation in this cluster.

The NGC 6366 data do not show significant star-to-star abundance variations or correlations for [Mg/Fe] and [Si/Fe], and from these data we can speculate that the gas from which

Table 7
Literature References

Stellar Population	Reference
HP-1	Barbuy et al. (2006)
NGC 6342	Origlia et al. (2005a)
NGC 6352	Feltzing et al. (2009)
NGC 6388	Carretta et al. (2007)
NGC 6388	Carretta et al. (2009b)
NGC 6388	Worley & Cottrell (2010)
NGC 6440	Origlia et al. (2008)
NGC 6441	Gratton et al. (2006)
NGC 6441	Gratton et al. (2007)
NGC 6441	Origlia et al. (2008)
NGC 6528	Carretta et al. (2001)
NGC 6528	Origlia et al. (2005a)
NGC 6539	Origlia et al. (2005b)
NGC 6553	Cohen et al. (1999)
NGC 6553	Meléndez et al. (2003)
NGC 6553	Alves-Brito et al. (2006)
NGC 6553	Johnson et al. (2014)
NGC 6569	Valenti et al. (2011)
NGC 6624	Valenti et al. (2011)
Terzan 5	Origlia et al. (2011)
Terzan 5	Origlia et al. (2013)
UKS 1	Origlia et al. (2005b)
Galactic Bulge	Alves-Brito et al. (2010)
Galactic Bulge	Gonzalez et al. (2011)
Galactic Bulge	Hill et al. (2011)
Galactic Bulge	Johnson et al. (2011)
Galactic Bulge	Johnson et al. (2012)
Galactic Bulge	Bensby et al. (2013)
Galactic Bulge	Johnson et al. (2013)
Galactic Bulge	Johnson et al. (2014)

the cluster stars formed did not reach temperatures hot enough to burn significant amounts of Mg into Al nor Al into Si. Previous observations of metal-rich ([Fe/H] $\gtrsim$ −1) globular clusters have noted similar trends of small [Mg/Fe], [Al/Fe], and/or [Si/Fe] star-to-star abundance dispersions, and several authors have suggested that the MgAl cycle may be less efficient at higher metallicities (e.g., Carretta et al. 2004, 2007, 2009a; O''connell et al. 2011; Cordero et al. 2014, 2015). Although larger samples are still needed, the observations of NGC 6342 and NGC 6366 provided here support this idea. The current work and literature data shown in Figure 5 suggest that most globular clusters with −0.7 $\lesssim$ [Fe/H] $\lesssim$ −0.4 have about the same [Mg/Fe] and [Si/Fe] distributions, regardless of the extent of their O–Na anti-correlations.

In Figure 6, we plot the median [X/Fe] ratios and dispersions as a function of [Fe/H] for NGC 6342, NGC 6366, and several other metal-rich ([Fe/H] $\gtrsim$ −1) bulge globular clusters available in the literature. We find that the median [X/Fe] ratios and dispersions of most elements in NGC 6342 and NGC 6366 are in good agreement with other similar metallicity globular clusters (see also Table 6). Although the similar abundance trends of most elements heavier than Na in Figure 6 suggest a common formation environment, the different [La/Fe] distributions may indicate a more heterogeneous formation process.

For example, NGC 6342, NGC 6366, and NGC 6388 (Carretta et al. 2007) all exhibit similarly enhanced [La/Fe] ratios; however, HP-1 (Barbuy et al. 2006) and NGC 6553 (Alves-Brito et al. 2006) have [La/Fe] $\lesssim$ 0. Barbuy et al. (2009)

noted a similar trend that stars in NGC 6522 were significantly more Ba/La-enhanced than those of HP-1 and NGC 6558, despite all three clusters sharing roughly similar [Fe/H], α-element, and O–Na distributions. Additionally, Gratton et al. (2006) found that bulge clusters largely exhibited similar abundance patterns, but that certain elements, such as Mn, may vary from cluster-to-cluster. Therefore, unlike the α-elements Mg, Si, and Ca, which appear similarly enhanced for nearly all metal-rich bulge clusters, the heavy elements may provide some discrimination regarding how, or where, inner Galaxy clusters formed. The current data are insufficient to provide any definitive links between bulge clusters with similar heavy element abundances, but increased sample sizes will aid in the interpretation of the observed cluster-to-cluster heavy element abundance variations.

5.3. Comparing Bulge Globular Clusters and Field Stars

For stars with [Fe/H] $\lesssim$ −0.4, previous investigations have largely found that the bulge globular cluster and field star populations share similar compositions (e.g., Carretta et al. 2001; Gratton et al. 2006; Gonzalez et al. 2011; Origlia et al. 2011; Johnson et al. 2014). Figure 6 and Table 6 indicate that NGC 6342 and NGC 6366 continue this trend, and that the clusters only show significantly different patterns for [Na/Fe] (larger dispersion) and [La/Fe] (higher abundances). The [O/Fe] dispersion may also be larger for some clusters compared to the field stars; however, the larger measurement errors of [O/Fe], especially for field stars with uncertain gravities, make it more difficult to disentangle real scatter from measurement errors.

The larger [Na/Fe] dispersions in NGC 6342, NGC 6366, and other metal-rich bulge clusters (e.g., Carretta et al. 2007; Gratton et al. 2007; Johnson et al. 2014), compared to similar metallicity bulge field stars, are not surprising and likely a result of self-enrichment processes occurring in the cluster environments. On the other hand, the enhanced [La/Fe] abundances found in NGC 6342, NGC 6366, and NGC 6388 (Carretta et al. 2007; Worley & Cottrell 2010) stars may be a reflection of the broader Galactic globular cluster trend. In general, globular clusters tend to exhibit [Ba/Fe] and [La/Fe] ratios[13] that increase between [Fe/H] = −2.5 and −1.5, and then remain enhanced at [Ba, La/Fe] ∼ +0.3 to at least [Fe/H] = −0.5 (e.g., James et al. 2004; D'Orazi et al. 2010). In contrast, bulge field stars show similar enhancements at [Fe/H] $\lesssim$ −1, but the [Ba/Fe] and [La/Fe] ratios begin to decline at higher metallicity (e.g., McWilliam et al. 2010; Bensby et al. 2011, 2013; Johnson et al. 2011; see also Figure 6). Therefore, the [Fe/H] ∼ −0.5 clusters NGC 6342, NGC 6366, and NGC 6388 exhibit [La/Fe] abundances that are more similar to those of bulge field stars with [Fe/H] $\lesssim$ −1. However, the different behavior of [Ba/Fe] and [La/Fe] between field and cluster stars of similar metallicity, at least between [Fe/H] = −1 and −0.4, suggests that the two populations experienced different formation and s-process enrichment histories.

For metallicities higher than [Fe/H] ∼ −0.4, some composition differences between bulge field and cluster stars may become more prevalent. In particular, Figure 6 indicates that [Mg/Fe], [Si/Fe], and [Ca/Fe] may remain enhanced to a higher

---

[13] Although Ba and La isotopes can be produced in both the r-process and s-process, at [Fe/H] $\gtrsim$ −1, and also in the solar system, these elements are predominantly produced by the s-process (e.g., see reviews by Busso et al. 1999; Sneden et al. 2008).
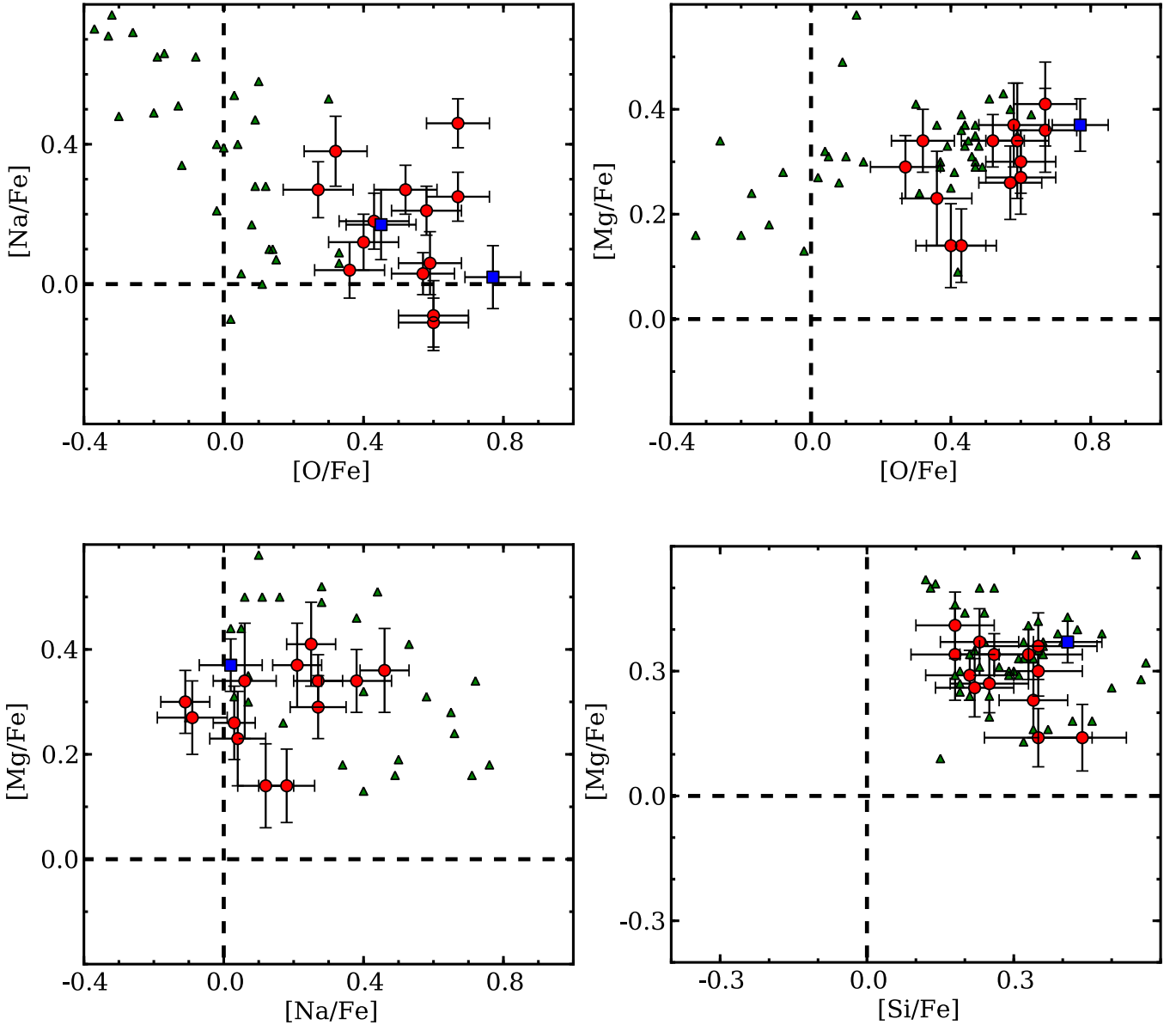
Figure 5. Similar to Figure 11 of Carretta (2015), plots of the O–Na, O–Mg, Na–Mg, and Si–Mg distributions are shown for NGC 6342 and NGC 6366. The dashed black lines indicate the solar abundances ratios, and the symbols are the same as those in Figure 3. The filled green triangles in each panel indicate the abundance ratios for individual stars of the bulge globular clusters listed in Table 7. For comparison purposes we have only included clusters that have [Fe/H] between −0.70 and −0.40, which are comparable to the metallicities of NGC 6342 and NGC 6366.

metallicity in cluster stars than bulge field stars (e.g., see also Carretta et al. 2007). Since the [α/Fe] ratios of most clusters remain approximately constant and enhanced, at least up to [Fe/H] ∼ −0.1, the data suggest a stronger contribution from core-collapse supernovae (e.g., Tinsley 1979), and possibly also a more rapid formation timescale, for the inner Galaxy cluster population. However, more globular cluster α-element abundance measurements, especially for clusters with [Fe/H] ≳ −0.3, are needed to definitively confirm that the most metal-rich globular clusters have higher [α/Fe] ratios than similar metallicity bulge field stars.

Among the heavier elements discussed here (Cr, Ni, and La), only the [La/Fe] ratios show any evidence of discriminating bulge cluster stars from field stars at [Fe/H] > −0.4. The data from NGC 6553 (Alves-Brito et al. 2006) shown in Figure 6 indicate marginally higher [La/Fe] abundances than the similar metallicity field stars. Similarly, Carretta et al. (2001) found the

near solar metallicity bulge cluster NGC 6528 to have an average [Ba/Fe] = +0.14, which is again marginally higher than the roughly solar [Ba/Fe] abundances found in micro-lensed bulge dwarf stars (Bensby et al. 2011, 2013).[14] Although more data comparing the heavy element abundance trends of metal-rich bulge cluster and field stars are needed, the small samples available so far indicate that the stronger s-process signature found in clusters near [Fe/H] = −0.5 may continue to at least solar metallicity.

Finally, a comparison between the chemical composition of bulge clusters with −1 ≲ [Fe/H] ≲ 0 and similar metallicity field stars suggests that the former population likely did not contribute a significant number of stars to the latter population.

---

[14] The reader should note that if the Carretta et al. (2001) data are compared with the Baade's window [Ba/Fe] abundances from McWilliam & Rich (1994), both populations exhibit similar [Ba/Fe] enhancements.
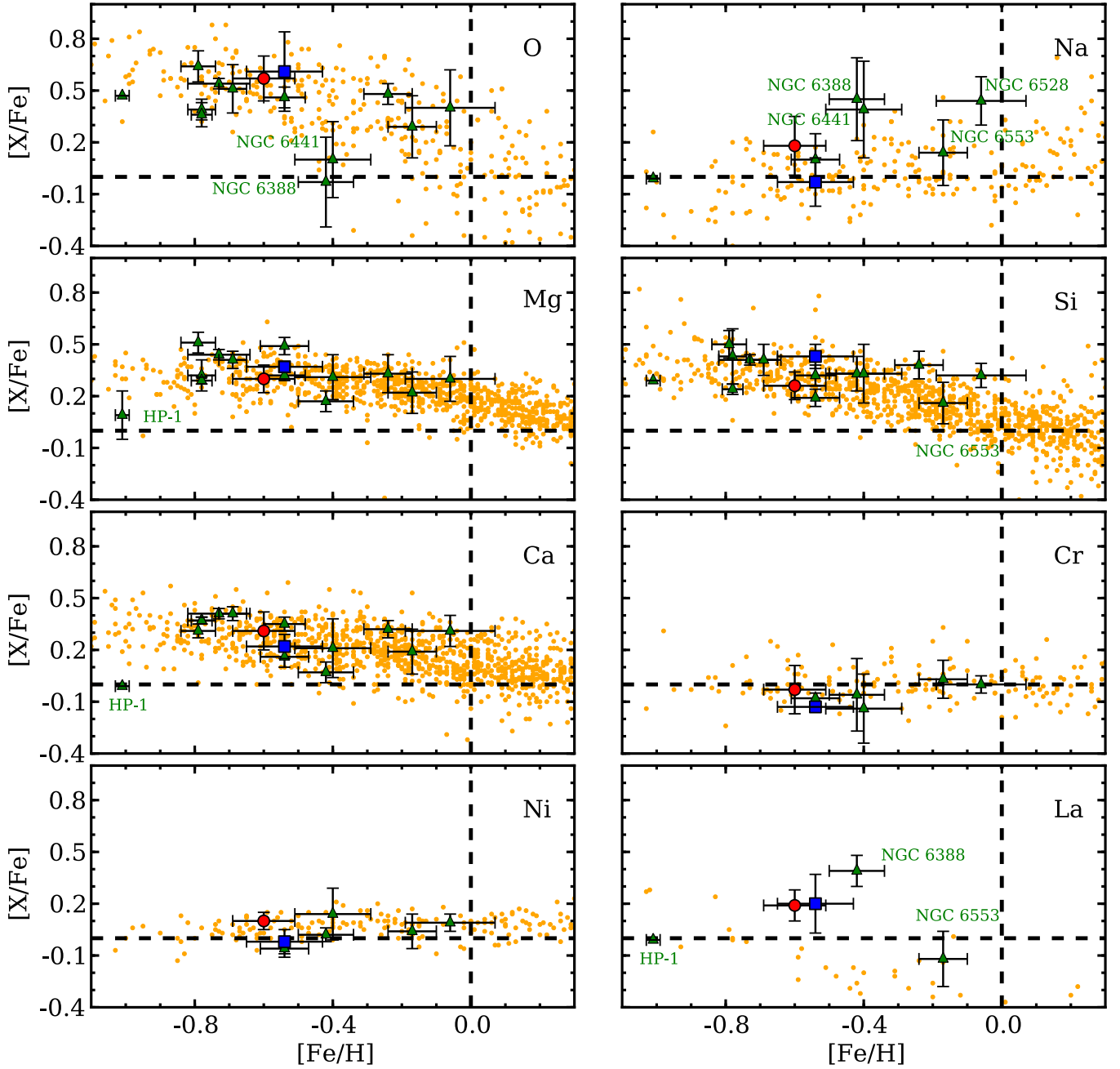
Figure 6. Panels compare the [X/Fe] ratios of NGC 6342 (filled blue squares) and NGC 6366 (filled red circles) as a function of [Fe/H] with bulge field star (filled orange circles) and bulge globular cluster (filled green triangles) data from the literature. The bulge globular cluster data are limited to those having $-1 \lesssim$ [Fe/H] $\lesssim 0$ and a Galactocentric distance ($R_{\rm GC}$) $\lesssim 5$ kpc. For all clusters, the symbols indicate the median abundance ratios and the error bars show the standard deviation. The literature references are provided in Table 7. Clusters of interest in each panel are identified by name (see text for details). For Terzan 5, only stars with [Fe/H] < 0 have been included, and the metal-poor ([Fe/H] ~ -0.8) and intermediate metallicity ([Fe/H] ~ -0.3) populations are shown as separate symbols.

Second generation stars from clusters such as NGC 6388 and NGC 6441 are strongly ruled out by their very low [O/Fe] and high [Na/Fe] ratios, and the clusters' first generation stars are incompatible with the field star composition based on their [La/Fe] abundances. More typical clusters such as NGC 6342 and NGC 6366 are ruled out mostly by their large [Na/Fe] spreads and enhanced [La/Fe] abundances. Similarly, clusters with [Fe/H] $\gtrsim -0.4$ are mostly ruled out by their higher [α/Fe] abundances compared to the field stars. Clusters such as Terzan 5 could have contributed stars to the bulge field (e.g., see Origlia et al. 2011, 2013), but it is not clear how many such objects exist nor is it clear that Terzan 5's composition will

remain compatible with the field once its [Na/Fe] and heavy element abundances are measured.

6. SUMMARY

For this project, we used the MMT–Hectochelle and WIYN–Hydra spectrographs to obtain high-resolution spectra of 267 RGB stars and 51 RGB stars in the bulge globular clusters NGC 6342 and NGC 6366, respectively. Cluster membership was determined primarily through radial velocity measurements. However, the significant reddening and stellar crowding along each cluster's line of sight reduced the member-to-target ratio to 8% for NGC 6342 and 37% for NGC 6366. The cluster

members provided average radial velocities of $+112.5\,\mathrm{km\,s^{-1}}$ ($\sigma = 8.6\,\mathrm{km\,s^{-1}}$) and $-122.3\,\mathrm{km\,s^{-1}}$ ($\sigma = 1.5\,\mathrm{km\,s^{-1}}$) for NGC 6342 and NGC 6366, respectively.

From the sub-sample of confirmed cluster members, we were able to measure chemical abundances of O, Na, Mg, Si, Ca, Cr, Fe, Ni, and La for four stars in NGC 6342 and 13 stars in NGC 6366 via EW measurements and spectrum synthesis fitting. We find both clusters to have nearly identical metallicities with NGC 6342 having $\langle[\mathrm{Fe/H}]\rangle = -0.53$ ($\sigma = 0.11$) and NGC 6366 having $\langle[\mathrm{Fe/H}]\rangle = -0.55$ ($\sigma = 0.09$). Neither cluster shows significant evidence favoring a metallicity spread. Both clusters exhibit very similar average $[\mathrm{X/Fe}]$ ratios and star-to-star abundance variations, but O and Na are likely the only two elements that exhibit significant star-to-star scatter. NGC 6366 shows evidence of only a moderately extended O–Na anti-correlation, but more data are needed for NGC 6342 to determine if this cluster also follows the same light element pattern. The lack of additional abundance correlations in NGC 6366 (e.g., Mg–Si correlation) indicates that the mechanism responsible for the O–Na anti-correlation did not reach temperatures high enough to significantly deplete Mg nor produce Si.

Although $[\mathrm{O/Fe}]$ is significantly enhanced ($[\mathrm{O/Fe}] > +0.50$) for most stars in our sample, the heavier α-elements have a more modest enhancement of $\langle[\alpha/\mathrm{Fe}]\rangle = +0.31$ ($\sigma = 0.06$). The Fe-peak elements Cr and Ni mostly track Fe, but there is some weak evidence that NGC 6366 may be slightly more enhanced in $[\mathrm{Cr/Fe}]$ and $[\mathrm{Ni/Fe}]$ than NGC 6342. Interestingly, NGC 6342 and NGC 6366 are both moderately enhanced in La with $\langle[\mathrm{La/Fe}]\rangle \sim +0.20$, which likely indicates some enrichment via the main s-process. When the abundance patterns of NGC 6342 and NGC 6366 are compared with those of other similar metal-rich ($[\mathrm{Fe/H}] > -1$) bulge clusters, we find that most metal-rich clusters share a common composition pattern. However, we find some evidence favoring significant cluster-to-cluster variations in $[\mathrm{La/Fe}]$, which could be an indication that inner Galaxy globular cluster formation was a more heterogeneous process than is reflected in the α-element chemistry.

A further comparison between metal-rich bulge globular clusters and bulge field stars with $[\mathrm{Fe/H}] < -0.4$ indicates that both populations exhibit nearly identical $[\alpha/\mathrm{Fe}]$, $[\mathrm{Cr/Fe}]$, and $[\mathrm{Ni/Fe}]$ abundance trends. However, the clusters are distinguished from the field stars by exhibiting larger $[\mathrm{O/Fe}]$ and $[\mathrm{Na/Fe}]$ dispersions, and also by their enhanced $[\mathrm{La/Fe}]$ abundances (for some clusters). At $[\mathrm{Fe/H}] > -0.4$, the most metal-rich globular clusters may be further distinguished from the bulge field stars by remaining enhanced in $[\alpha/\mathrm{Fe}]$ up to at least solar metallicity.

REFERENCES

Alonso, A., Salaris, M., Martinez-Roger, C., Straniero, O., & Arribas, S. 1997, A&A, 323, 374
Alonso-García, J., Mateo, M., Sen, B., et al. 2012, AJ, 143, 70
Alves-Brito, A., Barbuy, B., Zoccali, M., et al. 2006, A&A, 460, 269
Alves-Brito, A., Meléndez, J., Asplund, M., Ramírez, I., & Yong, D. 2010, A&A, 513, AA35
Arnould, M., Goriely, S., & Jorissen, A. 1999, A&A, 347, 572
Barbuy, B., Zoccali, M., Ortolani, S., et al. 2006, A&A, 449, 349
Barbuy, B., Zoccali, M., Ortolani, S., et al. 2009, A&A, 507, 405
Bellini, A., Piotto, G., Milone, A. P., et al. 2013, ApJ, 765, 32
Bensby, T., Adén, D., Meléndez, J., et al. 2011, A&A, 533, A134
Bensby, T., Yee, J. C., Feltzing, S., et al. 2013, A&A, 549, A147
Bershady, M., Barden, S., Blanche, P.-A., et al. 2008, Proc. SPIE, 7014, 70140H
Bica, E., Bonatto, C., Barbuy, B., & Ortolani, S. 2006, A&A, 450, 105
Busso, M., Gallino, R., & Wasserburg, G. J. 1999, ARA&A, 37, 239
Campos, F., Kepler, S. O., Bonatto, C., & Ducati, J. R. 2013, MNRAS, 433, 243
Carretta, E. 2015, ApJ, 810, 148
Carretta, E., Bragaglia, A., Gratton, R., & Lucatello, S. 2009a, A&A, 505, 139
Carretta, E., Bragaglia, A., Gratton, R. G., et al. 2007, A&A, 464, 967
Carretta, E., Bragaglia, A., Gratton, R. G., et al. 2009b, A&A, 505, 117
Carretta, E., Bragaglia, A., Gratton, R. G., et al. 2014, A&A, 564, A60
Carretta, E., Cohen, J. G., Gratton, R. G., & Behr, B. B. 2001, AJ, 122, 1469
Carretta, E., Gratton, R. G., Bragaglia, A., Bonifacio, P., & Pasquini, L. 2004, A&A, 416, 925
Casetti-Dinescu, D. I., Girard, T. M., Korchagin, V. I., van Altena, W. F., & López, C. E. 2010, AJ, 140, 1282
Castelli, F., & Kurucz, R. L. 2004, arXiv:astro-ph/0405087
Cohen, J. G., Gratton, R. G., Behr, B. B., & Carretta, E. 1999, ApJ, 523, 739
Cohen, J. G., & Kirby, E. N. 2012, ApJ, 760, 86
Cordero, M. J., Pilachowski, C. A., Johnson, C. I., & Vesperini, E. 2015, ApJ, 800, 3
Cordero, M. J., Pilachowski, C. A., Johnson, C. I., et al. 2014, ApJ, 780, 94
Côté, P. 1999, AJ, 118, 406
Da Costa, G. S., & Armandroff, T. E. 1995, AJ, 109, 2533
Da Costa, G. S., & Seitzer, P. 1989, AJ, 97, 405
D'Orazi, V., Gratton, R., Lucatello, S., et al. 2010, ApJL, 719, L213
Dotter, A., Chaboyer, B., Jevremović, D., et al. 2008, ApJS, 178, 89
Dotter, A., Sarajedini, A., Anderson, J., et al. 2010, ApJ, 708, 698
Dubath, P., Meylan, G., & Mayor, M. 1997, A&A, 324, 505
Feltzing, S., Primas, F., & Johnson, R. A. 2009, A&A, 493, 913
Ferraro, F. R., Dalessandro, E., Mucciarelli, A., et al. 2009, Natur, 462, 483
Forbes, D. A., & Bridges, T. 2010, MNRAS, 404, 1203
Freeman, K. C., & Norris, J. 1981, ARA&A, 19, 319
González Hernández, J. I., & Bonifacio, P. 2009, A&A, 497, 497
Gonzalez, O. A., Rejkuba, M., Zoccali, M., et al. 2011, A&A, 530, A54
Gratton, R., Sneden, C., & Carretta, E. 2004, ARA&A, 42, 385
Gratton, R. G., Carretta, E., & Bragaglia, A. 2012, A&ARv, 20, 50
Gratton, R. G., Lucatello, S., Bragaglia, A., et al. 2006, A&A, 455, 271
Gratton, R. G., Lucatello, S., Bragaglia, A., et al. 2007, A&A, 464, 953
Harris, W. E. 1996, AJ, 112, 1487
Heitsch, F., & Richtler, T. 1999, A&A, 347, 455
Hill, V., Lecureur, A., Gómez, A., et al. 2011, A&A, 534, A80
Hinkle, K., Wallace, L., Valenti, J., & Harmer, D. 2000, in Visible and Near Infrared Atlas of the Arcturus Spectrum 3727-9300 A, ed. K. Hinkle et al. (San Francisco, CA: ASP), 248
James, G., François, P., Bonifacio, P., et al. 2004, A&A, 427, 825
Johnson, C. I., & Pilachowski, C. A. 2010, ApJ, 722, 1373
Johnson, C. I., Rich, R. M., Fulbright, J. P., Valenti, E., & McWilliam, A. 2011, ApJ, 732, 108
Johnson, C. I., Rich, R. M., Kobayashi, C., et al. 2013, ApJ, 765, 157

Johnson, C. I., Rich, R. M., Kobayashi, C., & Fulbright, J. P. 2012, ApJ, 749, 175

Johnson, C. I., Rich, R. M., Kobayashi, C., Kunder, A., & Koch, A. 2014, AJ, 148, 67

Johnson, C. I., Rich, R. M., Pilachowski, C. A., et al. 2015, AJ, 150, 63

Johnson, H. R., Mould, J. R., & Bernat, A. P. 1982, ApJ, 258, 161

Knezek, P. M., Bershady, M. A., Willmarth, D., et al. 2010, Proc. SPIE, 7735, 77357D

Kraft, R. P. 1994, PASP, 106, 553

Kunder, A., Koch, A., Rich, R. M., et al. 2012, AJ, 143, 57

Langer, G. E., Hoffman, R., & Sneden, C. 1993, PASP, 105, 301

Lawler, J. E., Bonvallet, G., & Sneden, C. 2001, ApJ, 556, 452

Marín-Franch, A., Aparicio, A., Piotto, G., et al. 2009, ApJ, 694, 1498

Mauro, F., Moni Bidin, C., Cohen, R., et al. 2012, ApJL, 761, L29

McWilliam, A., Fulbright, J., & Rich, R. M. 2010, in IAU Symp. 265, Chemical Abundances in the Universe: Connecting First Stars to Planets, ed. K. Cunha, M. Spite, & B. Barbuy (Cambridge: Cambridge Univ. Press), 279

McWilliam, A., & Rich, R. M. 1994, ApJS, 91, 749

Meléndez, J., Asplund, M., Alves-Brito, A., et al. 2008, A&A, 484, L21

Meléndez, J., Barbuy, B., Bica, E., et al. 2003, A&A, 411, 417

Minniti, D. 1995, AJ, 109, 1663

Nataf, D. M., Gould, A. P., Pinsonneault, M. H., & Udalski, A. 2013, ApJ, 766, 77

Ness, M., Freeman, K., Athanassoula, E., et al. 2013, MNRAS, 432, 2092

O''connell, J. E., Johnson, C. I., Pilachowski, C. A., & Burks, G. 2011, PASP, 123, 1139

Origlia, L., Massari, D., Rich, R. M., et al. 2013, ApJL, 779, L5

Origlia, L., Rich, R. M., Ferraro, F. R., et al. 2011, ApJL, 726, L20

Origlia, L., Valenti, E., & Rich, R. M. 2005a, MNRAS, 356, 1276

Origlia, L., Valenti, E., & Rich, R. M. 2008, MNRAS, 388, 1419

Origlia, L., Valenti, E., Rich, R. M., & Ferraro, F. R. 2005b, MNRAS, 363, 897

Ortolani, S., Barbuy, B., Momany, Y., et al. 2011, ApJ, 737, 31

Ortolani, S., Bica, E., & Barbuy, B. 1997, MNRAS, 284, 692

Paust, N. E. Q., Aparicio, A., Piotto, G., et al. 2009, AJ, 137, 246

Piotto, G., Milone, A. P., Bedin, L. R., et al. 2015, AJ, 149, 91

Prantzos, N., Charbonnel, C., & Iliadis, C. 2007, A&A, 470, 179

Ramírez, I., & Allende Prieto, C. 2011, ApJ, 743, 135

Rich, R. M., Sosin, C., Djorgovski, S. G., et al. 1997, ApJL, 484, L25

Roederer, I. U., & Thompson, I. B. 2015, MNRAS, 449, 3889

Rossi, L. J., Ortolani, S., Barbuy, B., Bica, E., & Bonfanti, A. 2015, MNRAS, 450, 3270

Rutledge, G. A., Hesser, J. E., Stetson, P. B., et al. 1997, PASP, 109, 883

Ryde, N., Gustafsson, B., Edvardsson, B., et al. 2010, A&A, 509, A20

Sarajedini, A., Bedin, L. R., Chaboyer, B., et al. 2007, AJ, 133, 1658

Saviane, I., da Costa, G. S., Held, E. V., et al. 2012, A&A, 540, A27

Skrutskie, M. F., Cutri, R. M., Stiening, R., et al. 2006, AJ, 131, 1163

Sneden, C. 1973, ApJ, 184, 839

Sneden, C., Cowan, J. J., & Gallino, R. 2008, ARA&A, 46, 241

Sneden, C., Lucatello, S., Ram, R. S., Brooke, J. S. A., & Bernath, P. 2014, ApJS, 214, 26

Szentgyorgyi, A., Furesz, G., Cheimets, P., et al. 2011, PASP, 123, 1188

Tinsley, B. M. 1979, ApJ, 229, 1046

Valenti, E., Ferraro, F. R., & Origlia, L. 2004, MNRAS, 351, 1204

Valenti, E., Origlia, L., & Rich, R. M. 2011, MNRAS, 414, 2690

van den Bergh, S. 2003, ApJ, 590, 797

VandenBerg, D. A., Brogaard, K., Leaman, R., & Casagrande, L. 2013, ApJ, 775, 134

Ventura, P., D'Antona, F., Di Criscienzo, M., et al. 2012, ApJL, 761, L30

Worley, C. C., & Cottrell, P. L. 2010, MNRAS, 406, 2504

Yong, D., Grundahl, F., Nissen, P. E., Jensen, H. R., & Lambert, D. L. 2005, A&A, 438, 875

Yong, D., Roederer, I. U., Grundahl, F., et al. 2014, MNRAS, 441, 3396

Zinn, R. 1985, ApJ, 293, 424

Zoccali, M., Gonzalez, O. A., Vasquez, S., et al. 2014, A&A, 562, A66